

Effect of Activating a Nickel–Molybdenum Catalyst in an Anion Exchange Membrane Water Electrolyzer

Wonjae Lee,^{II} Hyebin Yun,^{II} Yongmin Kim,^{II} Sun Seo Jeon, Hoon Taek Chung,* Byungchan Han,* and Hyunjoo Lee*



Cite This: *ACS Catal.* 2023, 13, 11589–11597



Read Online

ACCESS |

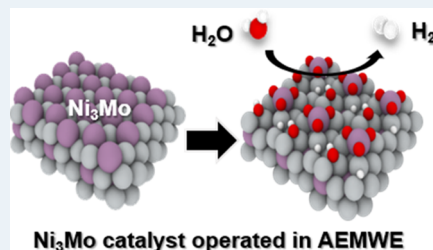
Metrics & More

Article Recommendations

Supporting Information

ABSTRACT: Water electrolysis using anion exchange membranes is promising for hydrogen production, and Ni–Mo catalysts have shown high activity for alkaline hydrogen evolution reaction (HER). However, their performance has been mostly tested in a half-cell setup and rarely studied in a single-cell setup with a membrane electrode assembly (MEA) structure, which is used for practical applications. With Ni₃Mo as the cathode, a single cell was fabricated using non-noble metal catalysts exclusively. Interestingly, the activation procedure significantly affected the cell performance. The single cell performed better than that with the Pt/C catalyst when the Ni₃Mo catalyst was mildly activated. The distribution of Mo in electrodes, membrane, and electrolytes was estimated, confirming Mo dissolution from the cathode. Once the cell was activated, the cell performance was stable without degradation in long-term chronopotentiometry operation, but the performance was degraded by sudden voltage change such as imposing open circuit voltage (OCV). The surface structure and reaction mechanism were studied with density functional theory: the Mo-dissolved Ni₃Mo(101) surface could promote H₂O dissociation, while MoO₃ stably adsorbed on the surface weakened H* adsorption, promoting HER. This study provides important insights into the development of efficient catalysts for large-scale hydrogen production.

KEYWORDS: nickel, molybdenum, hydrogen evolution reaction, anion exchange membrane water electrolyzer, activation



1. INTRODUCTION

Renewable energy sources like solar and wind energy are being used to replace fossil fuels.^{1–3} By electrolyzing water, energy can be stored in hydrogen, which can then be transported and used as needed.^{4–7} A water electrolyzer with a structure of cathode, polymer electrolyte, and anode has been actively investigated.^{8,9} A proton exchange membrane water electrolyzer (PEMWE) requires Ir, which is the rarest metal on earth, because it is the only stable catalyst under a highly acidic condition.¹⁰ An anion exchange membrane water electrolyzer (AEMWE), however, can work with a non-noble metal catalyst such as Ni, which considerably reduces the cost and enables large-scale hydrogen production.^{11–13}

When an anion exchange membrane is used, the cathodic reaction is $2\text{H}_2\text{O} + 2\text{e}^- \rightarrow 2\text{OH}^- + \text{H}_2$ and the anodic reaction is $2\text{OH}^- \rightarrow 1/2\text{O}_2 + \text{H}_2\text{O} + 2\text{e}^-$. Ni-based catalysts can catalyze both reactions.¹⁴ Ni–Fe layered double hydroxide (LDH) catalysts have presented high activity for anodic oxygen evolution reaction (OER). We previously reported that Ni–Fe LDH catalysts can be successfully applied in AEMWE.¹⁵ Ni–Mo catalysts have demonstrated high activity for hydrogen evolution reaction (HER).^{16–20} Jaramillo et al. nicely presented that Ni–Mo has the lowest overpotential in alkaline HER among various non-noble metal elements.²¹ However, these have been mostly performed in a half-cell setup with a three-electrode system consisting of working, counter, and

reference electrodes immersed in an aqueous electrolyte solution. It is common that the electrocatalyst with high activity in a half-cell setup presents poor performance in a single-cell partly because the single cell also suffers from various transport limitations. Still, it is crucial to test new catalysts in a single-cell setup with the membrane electrode assembly (MEA) structure for actual applications.

Here, we synthesized a Ni–Mo catalyst with various compositions, tested them in a half-cell setup, and fabricated a cathode using the catalyst showing the best activity in a half-cell. The Ni–Fe LDH catalyst was used as the anode, so the single-cell was made of non-noble metals only. Interestingly, the activation procedure affected the cell performance significantly, whereas Pt/C did not show such behavior. The single cell prepared with the Ni–Mo catalyst presented very good performance when mildly activated, and the cell performance was even better than the case with the Pt/C catalyst. Mo distribution in electrodes, membrane, and electrolytes was estimated, and the cell performance was

Received: May 28, 2023

Revised: August 7, 2023

Published: August 18, 2023



ACS Publications

© 2023 American Chemical Society

11589

<https://doi.org/10.1021/acscatal.3c02406>
ACS Catal. 2023, 13, 11589–11597

investigated under various conditions. The surface structure and reaction mechanism were elucidated with density functional theory (DFT) calculations.

2. EXPERIMENTAL SECTION

2.1. Chemicals. Nickel (II) chloride hexahydrate ($\text{NiCl}_2 \cdot 6\text{H}_2\text{O}$, 99.999% metal basis), molybdenum chloride (MoCl_5 , 95%), sodium hydroxide (NaOH , ≥ 97%), sodium carbonate (Na_2CO_3 , ≥ 99.5%), iron chloride (FeCl_3 , 97%), Nafion perfluorinated resin solution (5 wt % in lower aliphatic alcohols/water or 10 wt % in water), potassium molybdate (K_2MoO_4 , 98%), and poly(tetrafluoroethylene) (60 wt % in water) were purchased from Sigma-Aldrich. Pt/C (nominally 40% on carbon black powder) was purchased from Thermo Fisher Scientific. 2-propanol ($(\text{CH}_3)_2\text{CHOH}$, 99.7%) was purchased from Junsei. Sustainion membrane (X37-50 RT, $0.045 \Omega \text{ cm}^2$, thickness >50 μm) was purchased from Dioxide Materials. Potassium hydroxide solution and sodium nitrate (NaNO_3 , 98%) were purchased from Samchun Chemical. Carbon paper (Sigracet 39 BB) was purchased from Fuel Cell Store. Nickel foam (PPI 110) was purchased from TMAX.

2.2. Catalyst Synthesis. Ni–Mo catalysts were synthesized by co-precipitation with various molar ratios of Ni: Mo (1:1, 3:1, 4:1, and 6:1). For Ni_1Mo , a metal precursor solution was prepared by dissolving 1.78 g of $\text{NiCl}_2 \cdot 6\text{H}_2\text{O}$ and 2.05 g of MoCl_5 in 15 mL of deionized water. An alkaline solution was also prepared by dissolving 1.02 g of NaOH and 0.84 g of Na_2CO_3 in 15 mL of deionized water. These two solutions were mixed dropwise into 15 mL of deionized water to maintain a pH at ~8.5. This mixture was aged for 24 h under stirring, then washed, and dried. The prepared hydroxide powders were further reduced at 400 °C for 100 min in 10% H_2 (balance N_2). The catalysts with different Mo contents were prepared by adjusting the metal amount in metal precursor solution, while the other procedure was the same. Ni–Fe LDH was also synthesized using co-precipitation by following our previous paper.¹⁵ Briefly, 2.85 g of $\text{NiCl}_2 \cdot 6\text{H}_2\text{O}$ and 0.65 g of FeCl_3 were dissolved in 15 mL of deionized water, and 1.02 g of NaOH and 0.84 g of Na_2CO_3 were dissolved in 15 mL of deionized water. These two solutions were mixed dropwise to maintain a pH at ~8.5 and aged for 24 h under stirring. After washing and drying, the powder was ground and used for electrode preparation.

2.3. Characterizations. The actual content of Ni and Mo in the Ni–Mo catalyst was measured using inductively coupled plasma mass spectrometry (ICP-MS; Perkin Elmer NexION 1000). The Brunauer–Emmett–Teller (BET) surface area and pore volume were measured by N_2 adsorption and desorption with Micromeritics TriStar II 3020. X-ray photoelectron spectroscopy (XPS; Thermo VG Scientific, K-alpha) was used for measuring the surface composition of the catalysts and the electrodes. The C 1s peak was set at 284.6 eV as a reference in order to calibrate the binding energies. Scanning electron microscopy (SEM; Hitachi SU5000) and energy dispersive X-ray spectroscopy (EDS) was performed to observe the morphology and the electrode surface. Transmission electron microscopy (TEM; FEI Tecnai G2 F30 S-Twin) was also performed using a 300 kV electron beam. Portable X-ray fluorescence (XRF; Vanta Element) was used to analyze the amount of Mo on the cathode surface. The amount of Mo dissolved in the electrolyte was estimated using an inductively coupled plasma–optical emission spectrometer (ICP-OES; Thermo Scientific).

2.4. Electrochemical Measurement. Linear sweep voltammetry (LSV) was performed in a three-electrode cell using CHE760E (CH instruments). A catalyst ink was prepared by mixing 10 mg of the catalyst, 1 mL of deionized water, 1.5 mL of 2-propanol, and 60 μL of 5 wt % Nafion solution with an ionomer/catalyst (I/C) ratio of 0.32. The catalyst ink of 10 μL was loaded on a glassy carbon rotating disk electrode (RDE). LSV was measured from 0.15 to −0.5 V_{RHE} in the 1 M KOH solution. The MEA was fabricated using the Ni–Mo catalyst for cathode and Ni–Fe LDH for anode with the Sustainion membrane. For cathode, the Ni–Mo catalyst of 156 mg was mixed with 23.5 mL of 2-propanol, 7.2 mL of deionized water, and 0.17 mL of 20 wt % PTFE solution with an I/C ratio of 0.26. The cathode catalyst solution was sprayed on a carbon paper with a catalyst loading of 2.5 mg cm^{-2} . The cathode was calcined at 350 °C for 100 min to melt PTFE in the N_2 atmosphere. For the anode, Ni–Fe LDH (156 mg) was mixed with 23.5 mL of 2-propanol, 7.2 mL of deionized water, and 370 μL of 10 wt % Nafion solution with an I/C ratio of 0.26. The anode catalyst solution was sprayed on a Ni foam with a catalyst loading of 2.5 mg cm^{-2} . Before fabricating MEA, the Sustainion membrane was activated in the 1 M KOH solution for more than 50 h. The overall structure of the electrolyzer is shown in Figure S1. The single cell was operated at 50 °C with an active area of 5 cm^2 . The catholyte was 750 mL of 1 M KOH solution and the anolyte was 600 mL of 1 M KOH solution. Both electrolytes were separately circulated with a flow rate of 10 mL/min.

2.5. Computational Details. All calculations were carried out using first-principles DFT as implemented in the Vienna ab initio simulation package (VASP).²² The plane waves near the core region were replaced with pseudo potentials using a projector augmented wave (PAW) method to describe the interaction among core electrons.²³ The generalized gradient approximation (GGA) with the revised Perdew–Burke–Ernzerhof (RPBE) exchange-correlation functional was utilized.²⁴ Finally, the effect of solvent on the electrochemical properties of our system was predicted using VASPsol calculations.²⁵ The Kohn–Sham equation was expanded using the plane wave basis with a cutoff energy of 520 eV, and k -points were sampled using the $7 \times 7 \times 1$ Monkhorst–Pack mesh. The computational convergence was within 10^{-5} eV and 0.05 eV/ \AA for energy and force, respectively. A vacuum space of 15 \AA was inserted in a perpendicular direction to the surface model system to have little interaction with its images. A Pt(111) and Ni(111) surface were modeled using a slab of a 3×3 unit cell, and a $\text{Ni}_3\text{Mo}(101)$ surface was modeled using a slab of a 2×2 unit cell with five and six atomic layers, respectively.

Binding energies (E_b) of the Mo oxides and HER intermediate species were calculated by eq 1

$$E_b = E_{\text{adsorbate}/\text{catalyst}} - E_{\text{adsorbate}} - E_{\text{catalyst}} \quad (1)$$

where $E_{\text{adsorbate}/\text{catalyst}}$, $E_{\text{adsorbate}}$, and, E_{catalyst} correspond to the total energy of the catalyst adsorbed by chemical species on the surface, the total energy of an isolated adsorbate, and a clean catalyst, respectively. The more negative E_b indicates stronger adsorption. The reaction free energy of each step was calculated as $\Delta G = \Delta E + \Delta ZPE + T\Delta S - neU$, where ΔE is the internal energy change in the reaction and ΔZPE means zero-point energy correction predicted by the harmonic oscillator approximation, ΔS is entropic change through the reaction, U denotes an electrode potential referenced to the

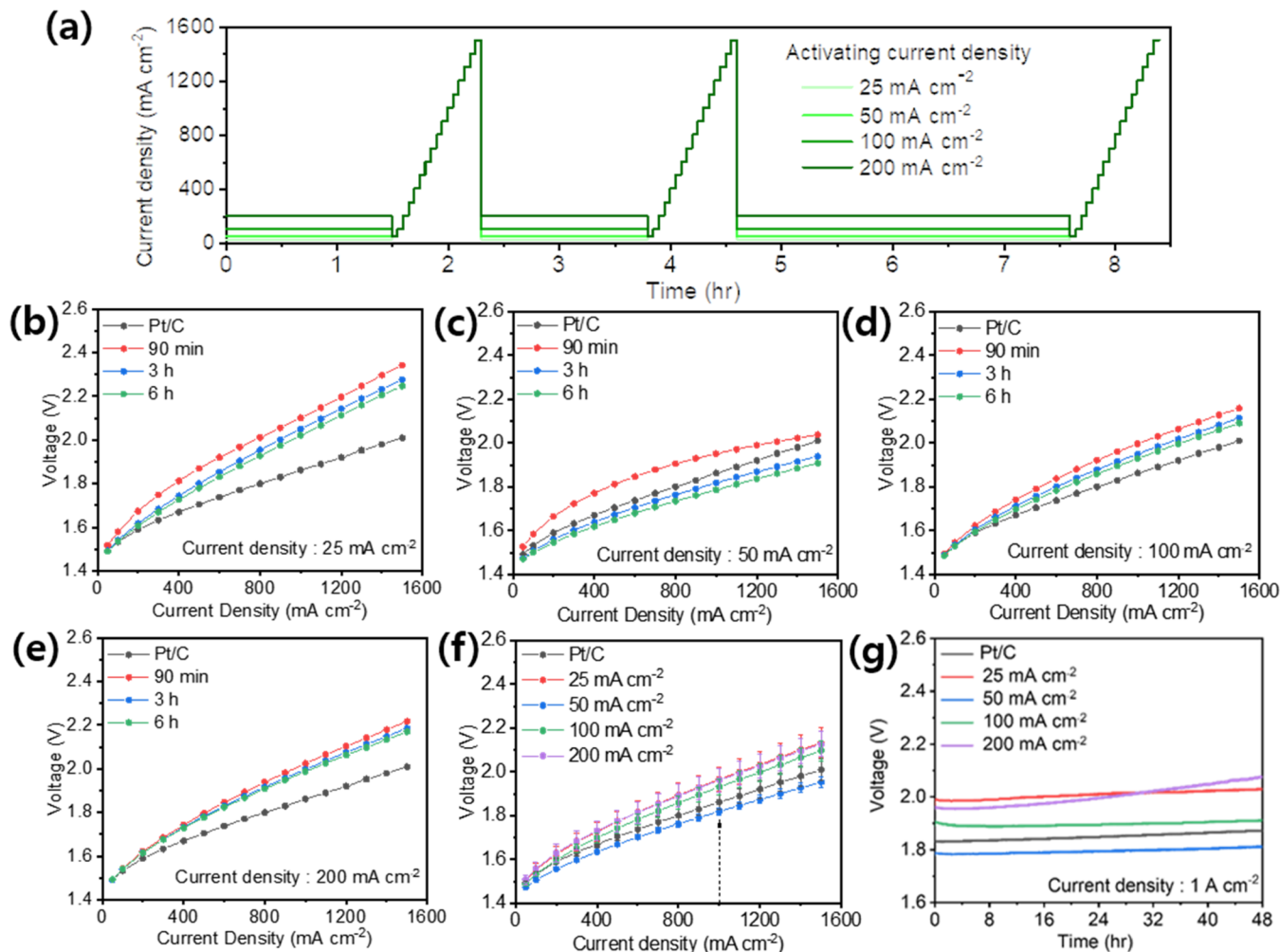


Figure 1. MEA test results using the Ni₃Mo catalyst for the cathode with various activation procedures. (a) Activation protocol; the steady current was applied to the cell with a current density of 25, 50, 100, and 200 mA cm⁻². A polarization was measured 3 times; first after 90 min of steady current flow, second after another 90 min, and third after additional 3 h. The polarization curves were shown when the current density applied for the activation was (b) 25, (c) 50, (d) 100, and (e) 200 mA cm⁻². (f) The comparison of the polarization curves activated for 6 h with different current densities. The measurement was repeated 4 times for each case to show error bars. (g) Durability test results by chronopotentiometry performed at 1 A cm⁻².

standard hydrogen electrode, and n is the number of electrons participating in the reaction. The transition metal atom vacancy formation energy on the catalyst surface E_f^v was computed according to the equation

$$E_f^v = E_v + \mu_i - E_0 \quad (2)$$

where E_v and E_0 are the total energy of the vacancy-containing and the initial configuration, respectively. μ_i is the chemical potential of the atom i removed from the initial structure that generates a vacancy.

3. RESULTS AND DISCUSSION

Ni–Mo catalysts were prepared by forming hydroxides with co-precipitation then reducing them under H₂ flow. Various compositions of Ni₁Mo, Ni₃Mo, Ni₄Mo, and Ni₆Mo were synthesized. ICP-MS results confirm that each catalyst has the desired composition (Table S1). SEM and TEM images show that all the catalysts have similar morphology (Figure S2). Ni₁Mo and Ni₃Mo have large BET surface area (61.8 and 66.5 m² g⁻¹, respectively), while Ni₄Mo and Ni₆Mo have significantly smaller BET surface area (42.8 and 32.4 m² g⁻¹,

respectively) (Table S1). The catalytic activity of these catalysts for HER was first evaluated in a half-cell setup with three electrodes and compared with the commercial 40 wt % Pt/C catalyst. Ni₃Mo catalysts showed the highest activity among various Ni–Mo catalysts; the potential at −10 mA cm⁻² was 160, 93, 98, and 137 mV_{RHE} for Ni₁Mo, Ni₃Mo, Ni₄Mo, and Ni₆Mo, respectively (Figure S3). The Pt/C still presented much better activity with a potential at −10 mA cm⁻² of 43 mV_{RHE}.

The Ni₃Mo catalyst was deposited on a carbon paper and applied for AEMWE as a cathode (Figure S1). Sustainion was used as a membrane, and Ni–Fe LDH was deposited on a Ni foam and used as an anode. On both electrodes, the precious metal catalysts were not used, instead Ni-based catalysts were used. A MEA was fabricated by sandwiching the membrane between the cathode and the anode. The catholyte and anolyte were separately circulated with a flow rate of 10 ml min⁻¹, and 1 M KOH aqueous solution was used as both electrolytes. The active electrode area was 5 cm², and the cell was operated at 50 °C. In order to activate the cell, chronopotentiometry was performed mildly at different current densities of 25, 50, 100,

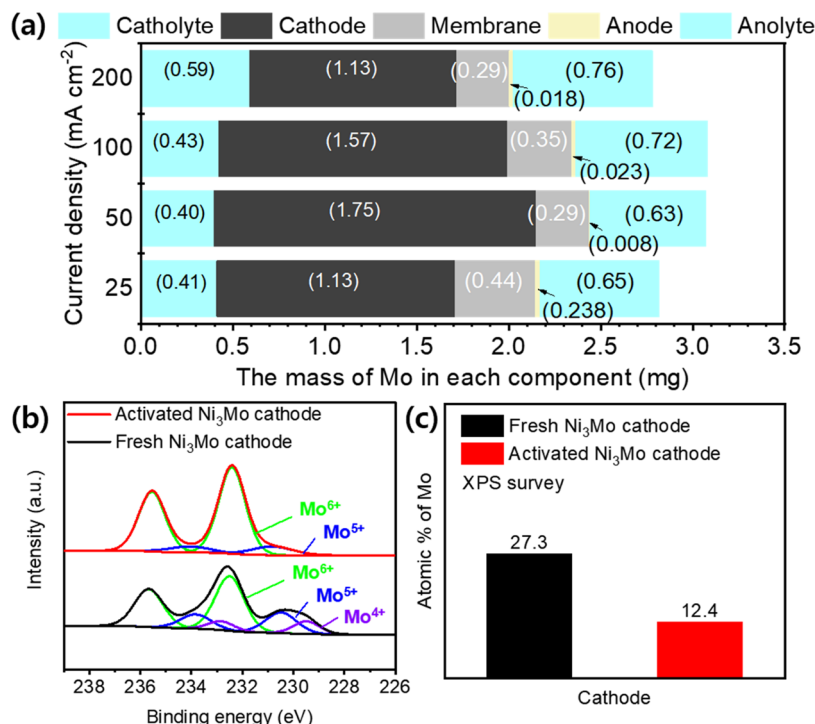


Figure 2. (a) Distribution of Mo species in each component of AEMWE for various activating current densities. Ni_3Mo catalyst was used for a cathode, and the activation was performed for 6 h. The Mo content in catholyte and anolyte was measured using ICP-OES. The Mo content in cathode, membrane, and anode was measured using XRF. The average values of four different sets were shown. (b) XPS Mo 3d spectra and (c) the atomic percentages of Mo measured by XPS of the Ni_3Mo cathode obtained before and after the activation with 50 mA cm^{-2} for 6 h.

and 200 mA cm^{-2} . The activation was performed for 90 min, and then the polarization curve was obtained by increasing the current density stepwise (Figure 1a). The current density increased up to 1500 mA cm^{-2} . Then, the chronopotentiometry was repeated for another 90 min, and a polarization curve was obtained again. This curve was denoted to have 3 h of activation. The chronopotentiometry was performed for another 3 h, and a polarization curve was obtained. This curve was denoted to have 6 h of activation.

As the activation time increased from 90 min to 3 and 6 h, the cell performance was enhanced for all the current densities (Figure 1b–e). When the current density used for activation was low such as 25 mA cm^{-2} , the polarization curve slowly reached the saturation. As the activating current density increased, the polarization curve reached the saturation faster. Interestingly, the saturated polarization curves present significant difference depending on the current density applied for activation. The polarization curves obtained after 6 h of activation were compared (Figure 1f). These cell tests were repeated 4 times for each case, and the variation was shown with error bars. The average polarization voltages were measured to be 1.47, 1.5, 1.55, and 1.61 V at the activating current densities of 25 , 50 , 100 , and 200 mA cm^{-2} , respectively. When the average cell voltage was compared at 1 A cm^{-2} in the polarization curves, it was 1.97, 1.82, 1.93, and 1.96 V for the activation current density of 25 , 50 , 100 , and 200 mA cm^{-2} , respectively. The cell voltage at 1 A cm^{-2} was 1.86 V in 40 wt % Pt/C. The activating current density of 50 mA cm^{-2} showed the best cell performance when the Ni_3Mo catalyst was used. In contrast, the Pt/C presented no difference for various activation times and activating current densities (Figure S4). The cell performance obtained with the activation current density of 50 mA cm^{-2} was even better than the Pt/C

with the same cathode catalyst loading. The durability of these MEAs was evaluated by performing chronopotentiometry at 1 A cm^{-2} . The cell voltage barely increased after 48 h of operation; the voltage increased from 1.78 to 1.81 V when the Ni_3Mo catalyst was activated at 50 mA cm^{-2} for 6 h prior to the durability test, and the voltage increased from 1.83 to 1.87 V in the Pt/C catalyst. The cell performance was maintained well once the cell was activated. When the Ni_3Mo catalyst was activated in a half-cell setup, the change in the activity was small when the activating current density or activating time was varied (Figure S5). In all cases, the activity was much poorer than the Pt/C catalyst.

The Mo distribution was estimated in each component of AEMWE after activation at various current densities for 6 h (Figure 2a). The Mo content in catholyte and anolyte was estimated by using ICP-OES, and the Mo content in cathode, membrane, and anode was estimated by XRF. The Mo mass of the fresh cathode before the activation was estimated as 3.3 mg by XRF, and Mo was not detected in all the other components. After the activation, a significant amount of Mo was dissolved out residing in the other components. The Mo species were observed in catholyte, cathode, membrane, and anolyte, but Mo was barely observed on the anode. The Mo content on the cathode was the highest as 1.75 mg when the activating current density was 50 mA cm^{-2} . The oxidation state of Mo was further investigated using XPS (Figure 2b). Although the fresh Ni_3Mo cathode contained various Mo oxidation states of Mo^{4+} , Mo^{5+} , and Mo^{6+} , the activated cathode had mostly Mo^{6+} species. The change in the Mo content at the electrode surface was also estimated from XPS. It also decreased significantly after the activation (Figure 2c). The cathode was also observed by SEM before and after the activation (Figure S6). There were more cracks after the activation, and the Mo

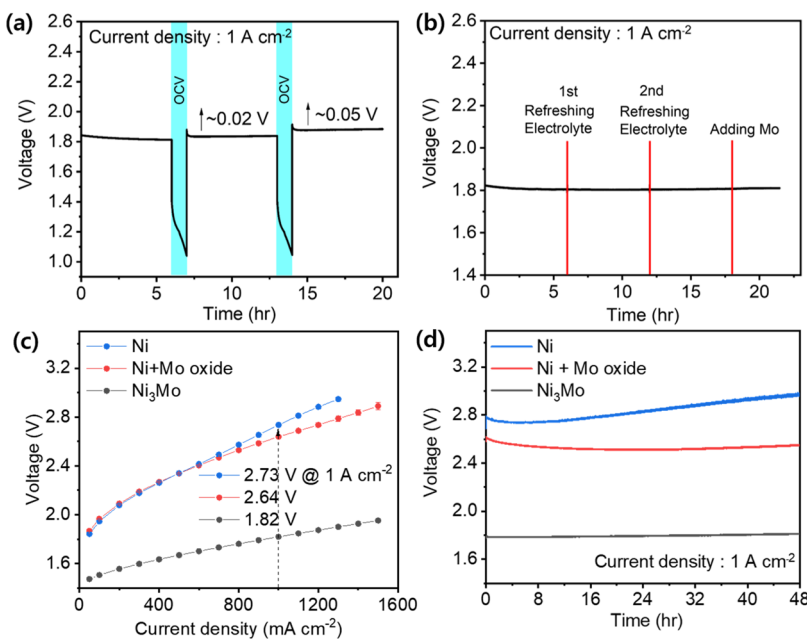


Figure 3. (a) Change in the cell voltage when OCV mode was imposed. The chronopotentiometry was performed for 6 h at 1 A cm^{-2} , then the OCV mode was imposed for 30 min. The same sequence was repeated twice. (b) The change in the cell voltage when the Mo concentration in the electrolyte was changed. The electrolytes were replaced into a fresh 1 M KOH solution after being operated for 6 h at 1 A cm^{-2} . After repeating this sequence once more, the Mo solution was added into the catholyte chamber. (c) Polarization curves when the Ni catalyst was used or when K_2MoO_4 salt was further added in the catholyte before activation. (d) Chronopotentiometry results at 1 A cm^{-2} for three cases as shown in panel (c). In all of the cases, the MEA was activated at 50 mA cm^{-2} for 6 h prior to the measurements.

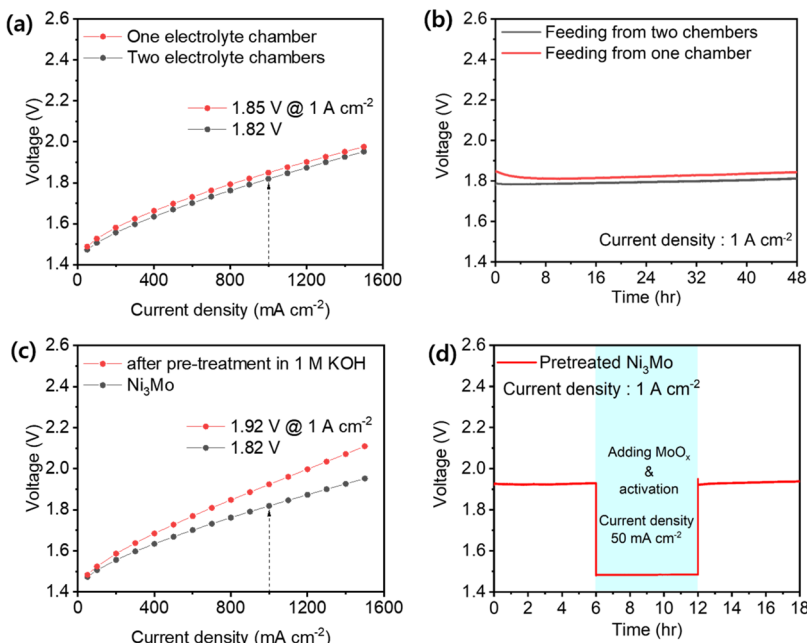
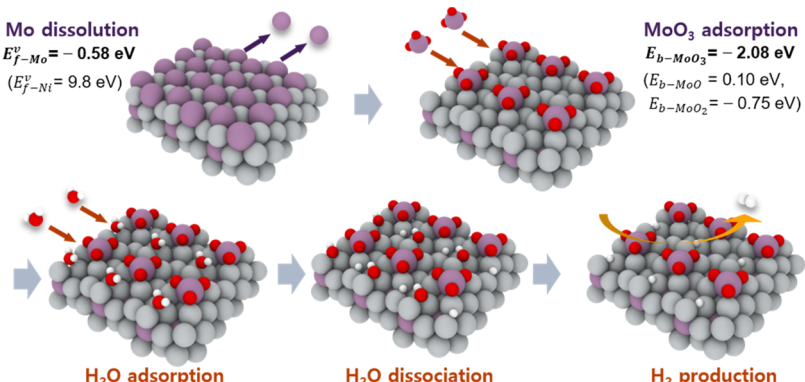


Figure 4. (a) Polarization curves and (b) chronopotentiometry results at 1 A cm^{-2} obtained when two electrolyte chambers were used for catholyte and anolyte, respectively, or when one electrolyte chamber was used for both electrolytes. (c) Polarization curves and (d) chronopotentiometry results at 1 A cm^{-2} obtained when Ni₃Mo catalyst was pretreated in 1 M KOH solution for 24 h. After 6 h of chronopotentiometry, the Mo solution (100 mg of K_2MoO_4 dissolved in 30 ml of 1 M KOH) was added, and then the activation was performed at 50 mA cm^{-2} for 6 h. The chronopotentiometry was obtained again at 1 A cm^{-2} for additional 6 h.

content also decreased significantly. The XRD pattern were obtained for the fresh Ni₃Mo catalyst and the cathode before and after HER (Figure S7). The peaks for NiO newly appear after the HER.

The operation of AEMWE was further investigated by observing the effect of voltage drop (Figure 3a). When the cell

was being operated stably at 1 A cm^{-2} , an open circuit voltage (OCV) mode was imposed for 30 min. The voltage dropped to $\sim 1 \text{ V}$. When the chronopotentiometry resumed at 1 A cm^{-2} , the voltage increased from 1.81 to 1.86 V then stabilized at 1.83 V. When the OCV mode was applied again, the voltage at 1 A cm^{-2} increased from 1.83 to 1.91 V then stabilized at 1.88

Scheme 1. Schematic Illustration of HER on $\text{MoO}_3/\text{Ni}_3\text{Mo}(101)$ in Alkaline Medium^a

^aThe $\text{Ni}_3\text{Mo}(101)$ surface is reconstructed by elemental Mo dissolution and redeposition as forms of Mo-containing oxides. DFT calculations indicate that water dissociation followed by H_2 production occurs at Ni sites. E_{FTM}^v means a vacancy formation (a point defect) energy on the catalyst surface. E_b is the binding energy of Mo oxide to the surface. The Ni, Mo, O, and H atoms are represented by gray, purple, red, and white spheres, respectively.

V. The electrode was being degraded upon sudden voltage change, possibly because the distribution of Mo species on the cathode was disturbed. On the other hand, the Mo concentration in the catholyte was changed by replacing the electrolyte, in which there were dissolved Mo species, into fresh electrolyte (Figure 3b). Particular attention was made to perform the chronopotentiometry steadily without disturbance in the current density. The electrolytes were replaced by connecting the circulating line of the electrolytes into a fresh 1 M KOH solution. No change in the cell voltage was observed. Then, K_2MoO_4 (100 mg) was dissolved in 30 ml of 1 M KOH solution, and this was added into the catholyte chamber. Still, no change in the cell voltage was observed. As long as the current density impeded on the MEA was constant, the change in the Mo concentration of the catholyte did not affect the cell performance.

The Ni catalyst was synthesized without a MoCl_3 precursor at otherwise the same synthesis condition as the Ni_3Mo catalyst, and its cell performance was evaluated (Figure 3c). The cell performance was quite poor with a cell voltage of 2.73 V at 1 A cm^{-2} . Additionally, K_2MoO_4 (5.9 mg) was dissolved in 50 mL of 1 M KOH solution, this Mo solution was added into the catholyte chamber, and the cell was activated at 50 mA cm^{-2} for 6 h. The cell performance was clearly improved with the cell voltage of 2.64 V at 1 A cm^{-2} , although it is still much worse than the case with the Ni_3Mo catalyst. This enhanced cell performance was maintained for 48 h as shown in the chronopotentiometry results (Figure 3d).

Different activation protocols were also applied by sweeping the voltage from 1.45 to 1.7 V or from 1.45 to 1.9 V (Figure S8). The polarization curves were obtained after 90 min, 3, and 6 h of activation. The cell voltage at 1 A cm^{-2} obtained after 6 h of activation was 1.91 V for the voltage sweep of 1.45–1.7 V and 2.03 V for 1.45–1.9 V. These activations by the voltage sweep were harsher than the chronopotentiometry, resulting in worse cell performance. On the other hand, the activation was performed at 25, 50, 100, and 200 mA cm^{-2} without obtaining the polarization curves in the middle for 6 h (Figure S9). The activating current density of 50 mA cm^{-2} still presented the best performance, but the differences among various current densities were smaller, indicating the importance of mild activation procedure.

Whether the catholyte and anolyte were circulated independently using two chambers or jointly using a single chamber, the effect of the number of electrolyte chambers was evaluated. (Figure 4a). The chronopotentiometry at 1 A cm^{-2} was also performed for 48 h in these two cases (Figure 4b). The cell performance was slightly better when two chambers were used, but the difference was marginal. The Ni_3Mo catalyst deposited on a carbon paper was immersed in the 1 M KOH solution for 24 h, then MEA was fabricated, and the cell performance was estimated (Figure 4c). The voltage at 1 A cm^{-2} was 1.92 V, which was significantly higher than 1.82 V in the case without pretreatment. Then, Mo species were added on the catholyte and activated again at 50 mA cm^{-2} (Figure 4d). However, the voltage was the same as before Mo addition. When the Ni_3Mo catalyst was properly activated, the MEA showed the best performance with the cell voltage of 1.82 V at 1 A cm^{-2} . The cell performance was worse when Mo was predissolved. The perturbation in the Mo concentration of the catholyte after the activation barely affected the cell performance.

First-principles DFT calculations were performed to identify the thermodynamically most feasible mechanism upon the structural reconstruction of the Ni_3Mo surface: elemental Mo dissolution followed by redeposition in the surface as Mo oxides (Scheme 1). Catalyst surfaces were modeled by $\text{Ni}(111)$, $\text{MoO}_3/\text{Ni}(111)$, $\text{Ni}_3\text{Mo}(101)$, and $\text{MoO}_3/\text{Ni}_3\text{Mo}(101)$ (Figure S10). The $\text{Ni}(111)$ surface, which is thermodynamically the most stable plane of a solid metallic Ni, was used as a reference system. The $\text{Ni}_3\text{Mo}(101)$ surface was selected considering that it is thermodynamically stable to be frequently observed in both experimental and theoretical studies.^{26,27}

DFT calculations indicated that the Mo vacancy formation in the $\text{Ni}_3\text{Mo}(101)$ surface is energetically spontaneous, implying that Mo dissolution into the electrolyte can be thermodynamically feasible. To identify the oxidation states of Mo in redepositing oxides to the $\text{Ni}_3\text{Mo}(101)$ surface, the binding energies of MoO_3 (Mo^{6+}), MoO_2 (Mo^{4+}), and MoO (Mo^{2+}) were calculated. It was obtained that MoO_3 adsorbs the most strongly with a binding energy of -2.08 eV , which is much stronger than MoO ($+0.10 \text{ eV}$) and MoO_2 (-0.75 eV). The results are consistent with our experimental observations

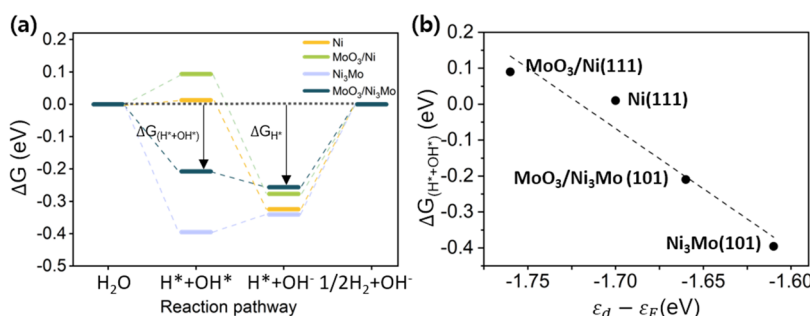


Figure 5. Theoretical prediction of HER activity. (a) Gibbs free energy diagram of HER on different catalyst surfaces. (b) Linear correlation between the derived $\Delta G_{(H^* + OH^*)}$ and $(\varepsilon_d - \varepsilon_F)$ of the catalyst; $\varepsilon_d - \varepsilon_F$ represents the d-band center energy relative to the Fermi level.

of the presence of Mo^{6+} species on the catalyst surface (Figure 2).

In addition to the DFT energetic argument on the surface reconstruction scenario, phase equilibria of solid metal, oxides, and ions were further evaluated using the Pourbaix diagram of Mo as a function of electrode potential and pH in the aqueous solution.²⁸ Especially, the Pourbaix diagram was investigated near the equilibrium boundary of hydrogen gas (H_2 (g)) and proton (H^+ , (aq)) in alkaline pH. In a bulk Mo Pourbaix diagram, metallic Mo is in thermodynamic equilibrium with MoO_4^{2-} (aq) in the alkaline solution. It is of interest to know how the phase equilibrium boundary shifts in the $Ni_3Mo(101)$ surface and where the new oxides are located. The equilibrium phase boundaries were calculated to identify feasible oxides around the HER regime using DFT calculations and the information in the bulk Mo Pourbaix diagram (Supporting Note 1 and Figure S11). The results were utilized for computational searching for the most plausible oxide phase depositing in the $Ni_3Mo(101)$ surface at pH = 14 (Figure S12). It was identified that MoO_3 was the most stable among MoO_3 , MoO_2 , and MoO in the potential window around where HER takes place. Our results indicate that the surface reconstruction begins with the electrochemical dissolution of Mo from the $Ni_3Mo(101)$ surface, followed by the redepositing MoO_3 at the defect site.

The dissolved Mo atoms would diffuse from the electrode surface to the membrane driven by the concentration gradient or chemical potential. Indeed, the presence of Mo ions near membrane was observed in our experimental results (Figure 2). The kinetic motion considerably depends on the ionic size and electrostatic interaction with chemical species in the diffusion medium. Considering that MoO_4^{2-} is quite a big ionic complex including solvation shells, there should be competition by two different driving forces: thermodynamic (diffusion from electrode into membrane) and kinetic (redepositing into the electrode). Hence, the dissolved Mo ions can be redeposited on the electrode surface if they are delayed to instantly move away from the electrodes. Our DFT calculations indicate that the adsorption of Mo oxides, rather than individual Mo atoms, exhibits thermodynamic feasibility on the vacant Mo sites on the electrode surface, forming dynamic active sites.

To understand the underlying mechanism of the apparent interplay of Ni–Mo alloying and MoO_3 adsorption on the HER catalytic performance, the key reaction steps were further analyzed using DFT calculations: (i) H_2O splitting into H^* and OH^* adsorption ($\Delta G_{(H^* + OH^*)}$) and (ii) desorption of OH^* left with adsorbed H^* (ΔG_{H^*}) in the catalyst surface (Figure 5). In the $MoO_3/Ni_3Mo(101)$, $\Delta G_{(H^* + OH^*)}$ was greatly

shifted into a more negative value of -0.21 eV (stronger adsorption) than in a pure $Ni(111)$ surface. ΔG_{H^*} was slightly more negative than $\Delta G_{(H^* + OH^*)}$ as -0.26 eV. The free energy landscape of $MoO_3/Ni_3Mo(101)$ is the most advantageous among the four catalysts. In fact, $\Delta G_{(H^* + OH^*)}$ is even better than Pt/C in HER catalysis (0.54 eV for Pt(111), Figure S13).

A linear relationship between $\Delta G_{(H^* + OH^*)}$ and the d-band center energy with respect to the Fermi level ($\varepsilon_d - \varepsilon_F$) is clearly shown in Figure 5b, as also reported previously.^{29–31} The stronger H_2O binding in the $Ni_3Mo(101)$ is attributed to the higher d-band center energy. The absence of Mo in the $Ni_3Mo(101)$ surface via Mo dissolution (Figure S10c) induced tensile strain on the surface, resulting in larger distances between neighboring Ni atoms (2.63 Å) than in the perfect $Ni(111)$ surface (2.48 Å). Consequently, the upshifted d-band center energy of the $Ni_3Mo(101)$ surface results in stronger H_2O adsorption, which promotes H_2O splitting into H^* and OH^* adsorption ($H^* + OH^*$). Both $Ni_3Mo(101)$ and $MoO_3/Ni_3Mo(101)$ surfaces were analyzed with various configurations of alkaline HER intermediates (Table S2). The results revealed that the active sites are predominantly Ni atoms, rather than Mo. Furthermore, the adsorbed MoO_3 downshifts the overall d-band center energy of the $Ni_3Mo(101)$ surface (Figure S14). As a result, the H_2O binding strength in $MoO_3/Ni_3Mo(101)$ surface is slightly weaker than in the $Ni_3Mo(101)$ surface, leading to the thermodynamically weaker H^* binding (ΔG_{H^*}) in the subsequent step. The H^* binding free energy (ΔG_{H^*}) of -0.26 eV for $MoO_3/Ni_3Mo(101)$ surface is closer to the optimal value ($\Delta G_{H^*} = 0$ eV) than any of the three catalysts. The energy difference between $\Delta G_{(H^* + OH^*)}$ and ΔG_{H^*} was only -0.05 eV, and it leads to a flat free energy diagram for the key HER step. Consequently, the theoretical findings demonstrate that the $MoO_3/Ni_3Mo(101)$ catalyst exhibits a synergistic effect of Mo-dissolved $Ni_3Mo(101)$ surface promoting H_2O dissociation and MoO_3 adsorption weakening the binding strength of H^* .

It is imperative to test the catalyst in the MEA setup for developing efficient water electrolyzers. Although many catalysts have been developed with high activity for HER or OER in a half-cell setup, their behavior was rarely studied in a single-cell setup. Here, we showed that the Ni_3Mo catalyst can present even better cell performance than the Pt/C catalyst as long as Ni_3Mo is activated mildly and the electrode voltage is stable. In order to estimate the effect of surface hydrophobicity or the electrode thickness on the cell performance, the contact angle (Figure S15) and electrode/catalyst layer thickness (Figure S16) were compared for the Pt/C and Ni_3Mo catalysts before and after HER. No significant difference was observed between the Pt/C and Ni_3Mo catalysts. DFT calculation

results show that MoO_3 species can exist stably in highly alkaline condition near the voltage where HER occurs, and the Ni surface with redeposited MoO_3 species can be an even more efficient catalyst than Pt/C. It seems that these active sites can be formed more when the Ni_3Mo MEA cell was mildly activated.

4. CONCLUSIONS

Ni–Mo catalysts were synthesized with various compositions, and the Ni_3Mo catalyst showed the best HER performance in a half-cell setup. This catalyst was applied in a single-cell setup with a MEA structure. Interestingly, the cell performance varied greatly depending on how the cell was activated. When the cell was mildly activated by imposing the current density of 50 mA cm^{-2} for 6 h, the cell showed the best performance with 1.82 V at 1 A cm^{-2} , which was better than that of the 40 wt % Pt/C catalyst. It was found that a significant amount of Mo was dissolved out from the cathode to the other parts of the cell. The amount of residual Mo on the cathode was the largest at the activation current density of 50 mA cm^{-2} . Once the cell was activated, the cell performance was stable without degradation, regardless of the change in Mo concentration in the catholyte. However, the cell performance was degraded by a sudden voltage change such as imposing OCV. DFT calculation informed that Mo is being dissolved from the surface of Ni_3Mo , but redeposition of MoO_3 onto the surface is thermodynamically favored. Water dissociation is promoted on the Mo-dissolved Ni_3Mo surface, and the adsorbed MoO_3 species weaken the H adsorption, enhancing HER. This work provides a valuable insight about how a nonprecious Ni-based catalyst behaves in AEMWE, thus contributing to realizing more sustainable energy production.

■ ASSOCIATED CONTENT

SI Supporting Information

The Supporting Information is available free of charge at <https://pubs.acs.org/doi/10.1021/acscatal.3c02406>.

Description about DFT calculation for how to find the Pourbaix diagram (Supporting note 1); and additional data (Tables S1 and S2 and Figures S1–S16) ([PDF](#))

■ AUTHOR INFORMATION

Corresponding Authors

Hoon Taek Chung – Hanwha Solutions, Daejeon 34128, Republic of Korea; Email: hoon.chung@hanwha.com

Byungchan Han – Department of Chemical and Biomolecular Engineering, Yonsei University, Seoul 03722, Republic of Korea; [ORCID](#) 0000-0002-2325-6733; Email: bchan@yonsei.ac.kr

Hyunjoo Lee – Department of Chemical and Biomolecular Engineering, Korea Advanced Institute of Science and Technology, Daejeon 34141, Republic of Korea; [ORCID](#) 0000-0002-4538-9086; Email: azhyun@kaist.ac.kr

Authors

Wonjae Lee – Department of Chemical and Biomolecular Engineering, Korea Advanced Institute of Science and Technology, Daejeon 34141, Republic of Korea; [ORCID](#) 0009-0009-9279-551X

Hyebin Yun – Department of Chemical and Biomolecular Engineering, Yonsei University, Seoul 03722, Republic of Korea

Yongmin Kim – Department of Chemical and Biomolecular Engineering, Yonsei University, Seoul 03722, Republic of Korea; Hanwha Solutions, Daejeon 34128, Republic of Korea; [ORCID](#) 0009-0006-8414-4897

Sun Seo Jeon – Department of Chemical and Biomolecular Engineering, Korea Advanced Institute of Science and Technology, Daejeon 34141, Republic of Korea; [ORCID](#) 0000-0002-1073-1371

Complete contact information is available at: <https://pubs.acs.org/10.1021/acscatal.3c02406>

Author Contributions

W.L., H.Y., and Y.K. contributed equally to this work.

Notes

The authors declare no competing financial interest.

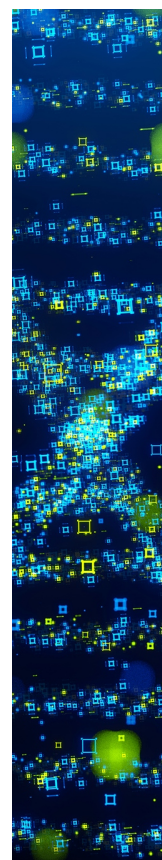
■ ACKNOWLEDGMENTS

This research was financially supported by the National Research Foundation of Korea (NRF-2021R1A3B1076715 and RS-2023-00229679) and Hanwha Solutions. We appreciate KARA (KAIST Analysis center for Research Advancement) for equipment.

■ REFERENCES

- 1 Abbasi, R.; Setzler, B. P.; Lin, S.; Wang, J.; Zhao, Y.; Xu, H.; Pivarov, B.; Tian, B.; Chen, X.; Wu, G.; Yan, Y. A roadmap to low-cost hydrogen with hydroxide exchange membrane electrolyzers. *Adv. Mater.* **2019**, *31*, No. 1805876.
- 2 Odenweller, A.; Ueckerdt, F.; Nermet, G. F.; Jensterle, M.; Luderer, G. Probabilistic feasibility space of scaling up green hydrogen supply. *Nat. Energy* **2022**, *7*, 854–865.
- 3 Kim, Y.; Jung, S.-M.; Kim, K.-S.; Kim, H.-Y.; Kwon, J.; Lee, J.; Cho, H.-S.; Kim, Y.-T. Cathodic protection system against a reverse-current after shut-down in zero-gap alkaline water electrolysis. *JACS Au* **2022**, *2*, 2491–2500.
- 4 Terlouw, T.; Bauer, C.; McKenna, R.; Mazzotti, M. Large-scale hydrogen production via water electrolysis: a techno-economic and environmental assessment. *Energy Environ. Sci.* **2022**, *15*, 3583–3602.
- 5 Seh, Z. W.; Kibsgaard, J.; Dickens, C. F.; Chorkendorff, I.; Norskov, J. K.; Jaramillo, T. F. Combining theory and experiment in electrocatalysis: insights into materials design. *Science* **2017**, *355*, No. eaad4998.
- 6 Zhu, Z.; Jiang, T.; Sun, J.; Liu, Z.; Xie, Z.; Liu, S.; Meng, Y.; Peng, Q.; Wang, W.; Zhang, K.; Liu, H.; Yuan, Y.; Li, K.; Chen, W. pH-Universal decoupled water electrolysis enabled by electrocatalytic hydrogen gas capacitive chemistry. *JACS Au* **2023**, *3*, 488–497.
- 7 Sharma, P.; Han, J.; Park, J.; Kim, D. Y.; Lee, J.; Oh, D.; Kim, N.; Seo, D.-H.; Kim, Y.; Kang, S. J.; Hwang, S. M.; Jang, J.-W. Alkali-metal-mediated reversible chemical hydrogen storage using seawater. *JACS Au* **2021**, *1*, 2339–2348.
- 8 Ajanovic, A.; Sayer, M.; Haas, R. The economics and the environmental benignity of different colors of hydrogen. *Int. J. Hydrogen Energy* **2022**, *47*, 24136–24154.
- 9 Kang, S. Y.; Park, J. E.; Jang, G. Y.; Kim, O.-H.; Kwon, O. J.; Cho, Y.-H.; Sung, Y.-E. High-performance and durable water electrolysis using a highly conductive and stable anion-exchange membrane. *Int. J. Hydrogen Energy* **2022**, *47*, 9115–9126.
- 10 Lim, J.; Kang, G.; Lee, J. W.; Jeon, S. S.; Jeon, H.; Kang, P. W.; Lee, H. Amorphous Ir atomic clusters anchored on crystalline IrO_2 nanoneedles for proton exchange membrane water oxidation. *J. Power Sources* **2022**, *524*, No. 231069.
- 11 Yu, Z.-Y.; Duan, Y.; Feng, X.-Y.; Yu, X.; Gao, M.-R.; Yu, S.-H. Clean and affordable hydrogen fuel from alkaline water splitting: past,

- recent progress, and future prospects. *Adv. Mater.* **2021**, *33*, No. 2007100.
- (12) Miller, H. A.; Bouzek, K.; Hnat, J.; Loos, S.; Bernacker, C. I.; Weibgarber, T.; Rontzsch, L.; Meier-Haack, J. Green hydrogen from anion exchange membrane water electrolysis: a review of recent developments in critical materials and operating conditions. *Sustainable Energy Fuels* **2020**, *4*, 2114–2133.
- (13) Li, D.; Motz, A. R.; Bae, C.; Fujimoto, C.; Yang, G.; Zhang, F.-Y.; Ayers, K. E.; Kim, Y. S. Durability of anion exchange membrane water electrolyzers. *Energy Environ. Sci.* **2021**, *14*, 3393–3419.
- (14) Sheng, W.; Myint, M.; Chen, J. G.; Yan, Y. Correlating the hydrogen evolution reaction activity in alkaline electrolytes with the hydrogen binding energy on monometallic surfaces. *Energy Environ. Sci.* **2013**, *6*, 1509–1512.
- (15) Jeon, S. S.; Lim, J.; Kang, P. W.; Lee, J. W.; Kang, G.; Lee, H. Design of principles of NiFe-Layered Double Hydroxide anode catalysts for anion exchange membrane water electrolyzers. *ACS Appl. Mater. Interfaces* **2021**, *13*, 37179–37186.
- (16) Xu, J. L.; Li, L. L.; Tang, J.; Dai, L.; Li, X. B.; Ye, Z. G.; Luo, J. M. Powder metallurgy synthesis of porous NiMo alloys as efficient electrocatalysts to enhance the hydrogen evolution reaction. *J. Alloys Compd.* **2021**, *865*, No. 158901.
- (17) Zhang, J.; Wang, T.; Liu, P.; Liao, Z.; Liu, S.; Zhuang, X.; Chen, M.; Zschech, E.; Feng, X. Efficient hydrogen production on MoNi₄ electrocatalysts with fast water dissociation kinetics. *Nat. Commun.* **2017**, *8*, No. 15437.
- (18) Wang, M.; Yang, H.; Shi, J.; Chen, Y.; Zhou, Y.; Wang, L.; Di, S.; Zhao, X.; Zhong, H.; Cheng, T.; Zhou, W.; Li, Y. Alloying Nickel with molybdenum significantly accelerates alkaline hydrogen electrocatalysis. *Angew. Chem. Int. Ed.* **2021**, *133*, 5835–5841.
- (19) Du, W.; Shi, Y.; Zhou, W.; Yu, Y.; Zhang, B. Unveiling the in situ dissolution and polymerization of Mo in Ni₄Mo alloy for promoting the hydrogen evolution reaction. *Angew. Chem. Int. Ed.* **2021**, *60*, 7051–7055.
- (20) Rößner, L.; Schwarz, H.; Veremchuk, I.; Zerdoumi, R.; Seyller, T.; Armbruster, M. Challenging the durability of intermetallic Mo-Ni compounds in the hydrogen evolution reaction. *ACS Appl. Mater. Interfaces* **2021**, *13*, 23616–23626.
- (21) McCrory, C. C. L.; Jung, S.; Ferrer, I. M.; Chatman, S. M.; Peters, J. C.; Jaramillo, T. F. Benchmarking hydrogen evolving reaction and oxygen evolving reaction electrocatalysts for solar water splitting devices. *J. Am. Chem. Soc.* **2015**, *137*, 4347–4357.
- (22) Hafner, J. Ab-initio simulations of materials using VASP: density-functional theory and beyond. *J. Comput. Chem.* **2008**, *29*, 2044–2078.
- (23) Blöchl, P. E. Projector augmented-wave method. *Phys. Rev. B* **1994**, *50*, 17953–17979.
- (24) Hammer, B.; Hansen, L. B.; Nørskov, J. K. Improved adsorption energetics within density-functional theory using revised Perdew-Burke-Ernzerhof functionals. *Phys. Rev. B* **1999**, *59*, 7413–7421.
- (25) Mathew, K.; Sundararaman, R.; Letchworth-Weaver, K.; Arias, T.; Hennig, R. G. Implicit solvation model for density-functional study of nanocrystal surfaces and reaction pathways. *J. Chem. Phys.* **2014**, *140*, No. 084106.
- (26) Pham, N. N.; Kang, S. G.; Kim, H.-J.; Pak, C.; Han, B.; Lee, S. G. Catalytic activity of Ni₃Mo surfaces for hydrogen evolution reaction: a density functional theory approach. *Appl. Surf. Sci.* **2021**, *537*, No. 147894.
- (27) Jian-Min, Z.; Fei, M.; Ke-Wei, X. Calculation of the surface energy of FCC metals with modified embedded-atom method. *Chin. Phys.* **2004**, *13*, 1082–1090.
- (28) Nikolaychuk, P. A.; Tyurin, A. G. The revised Pourbaix diagram for molybdenum. *HMo* **2011**, *24*, 101–105.
- (29) Wang, J.; Zhang, Z.; Song, H.; Zhang, B.; Liu, J.; Shai, X.; Miao, L. Water dissociation kinetic-oriented design of nickel sulfides via tailored dual sites for efficient alkaline hydrogen evolution. *Adv. Funct. Mater.* **2021**, *31*, No. 2008578.
- (30) Kang, W. J.; Feng, Y.; Li, Z.; Yang, W. Q.; Cheng, C. Q.; Shi, Z. Z.; Yin, P. F.; Shen, G. R.; Yang, J.; Dong, C. K.; et al. Strain-activated copper catalyst for pH-universal hydrogen evolution reaction. *Adv. Funct. Mater.* **2022**, *32*, No. 2112367.
- (31) Hu, Q.; Gao, K.; Wang, X.; Zheng, H.; Cao, J.; Mi, L.; Huo, Q.; Yang, H.; Liu, J.; He, C. Subnanometric Ru clusters with upshifted D band center improve performance for alkaline hydrogen evolution reaction. *Nat. Commun.* **2022**, *13*, No. 3958.



CAS BIOFINDER DISCOVERY PLATFORM™

STOP DIGGING THROUGH DATA — START MAKING DISCOVERIES

CAS BioFinder helps you find the right biological insights in seconds

Start your search

